Available online at www.sciencedirect.com
ScienceDirect
Journal of Magnetic Resonance 187 (2007) 1–9
JMR Journal of Magnetic Resonance
www.elsevier.com/locate/jmr

Simulation of 4D spectral-spatial EPR images

Kang-Hyun Ahn [a,b], Howard J. Halpern [a,b,*]

[a] Department of Radiation and Cellular Oncology, University of Chicago, Chicago, IL, USA
[b] Center for EPR Imaging in Vivo Physiology, University of Chicago, Chicago, IL, USA

Received 29 September 2006; revised 23 February 2007
Available online 1 March 2007

Abstract

Electron paramagnetic resonance imaging (EPRI) can be modeled by the forward projection of a 4D synthetic spectral-spatial phantom. We developed a simulation tool for EPRI and carried out a quantitative comparison between simulation and experiment, focusing on the signal and noise characteristics. The signal height in the simulation was compared to that in the experimental projections at gradients of different magnitudes and directions. We investigated the noise power spectrum of an EPR imager and incorporated it into the simulation. The signal and noise modeling of the simulation achieved the same performance as the EPR imager. Using this simulation, various sampling schemes were tried to find an optimized parameter set under the customized noise model of this EPR imager.

Keywords: EPR; 4D EPRI; Tomography; Spectral-spatial imaging; Simulation

1. Introduction

Electron paramagnetic resonance (EPR) experiments measure the resonant absorption of radiofrequency radiation by unpaired electrons in the presence of an external magnetic field. Obtaining projections by sweeping the magnetic field in the presence of an static linear gradients distinguishes paramagnetic signals according to their spatial positions, and achieves EPR imaging (EPRI). With three sets of gradient coils, one can impose equal-amplitude gradients over the angles subtending the unit sphere to reconstruct a 3D spatial distribution of spins in the object. The tomographic image reconstruction technique can be extended to an additional spectral dimension by scanning the gradient amplitude to produce a spectral-spatial image [1–3]. When the object of the spectral-spatial EPRI is a living animal, the spectral dimension provides useful information regarding the localized spectral shape of injected spin probes [4–7]. This process is mathematically described as a 4D Radon transform [8]. It can be modeled by the forward projection of a 4D synthetic spectral-spatial phantom.

Spectral-spatial EPRI has unique characteristics of resolution, signal-to-noise ratio (SNR), and systematic image artifacts, which involve multiple sources. It is well known that the SNR decreases with the increase in the gradient amplitude. Application of a field gradient over a distribution of spins broadens the spectral lines and reduces their signal heights. The low SNR at high gradient is partially compensated for by signal averaging. A quantitative understanding of the dependence of the signal height on the spatial spin distribution and gradient strength can be established through simulation. Besides the signal height variation, EPRI has complicated artifacts that depend on various mechanisms including spin physics, imager electronics, the physiology of imaged animals, and aspects of the reconstruction algorithm. To gain insight into these mechanisms, we need a tool that can selectively emphasize the effect from a particular source. Simulation of EPRI with various sets of controlled parameters is a powerful trouble shooting tool that can analyze artifacts from specified sources.

In this work, we validate the signal height variation in the simulation by comparing it with experimental projec-

* Corresponding author. Address: Department of Radiation and Cellular Oncology, MC1105, University of Chicago Medical Center, 5841 S. Maryland Ave., Chicago, IL 60637, USA. Fax: +1 773 702 5940.
E-mail address: h-halpern@uchicago.edu (H.J. Halpern).

1090-7807/$ - see front matter © 2007 Elsevier Inc. All rights reserved.
doi:10.1016/j.jmr.2007.02.013

tions obtained with gradients of different magnitudes and directions. The noise power spectrum was measured from our EPR imager and was incorporated into the simulation to closely follow the experimental SNR. The simulation with the proper signal and noise model can be used to verify experimental results. A systematic repetition of imaging with assured reproducibility allows fine-tuning of EPRI. We tried various sampling schemes in the search for an optimized parameter set. The performance of EPRI was characterized in two ways. The spectral dimension from each voxel of the image of a homogeneous phantom was fit to an accurate parametric spectral shape [9,10], which produces a 3D EPR line width image. The integrated EPR line (used in image reconstruction) is a single, centered narrow line. We define signal height as the spectral amplitude of the absorption line shape at the center bin of the magnetic field sweep dimension of our image. A 3D EPR signal height image is produced from every signal height of the localized spectrum associated with each spatial voxel of the 4D image. One criterion by which to judge a parameter set was the spatial resolution of the signal height image. The other criterion was the standard deviation of the spectral line width distribution. The simulation results provided a relationship between the field interval swept (sweep width) and the accuracy of the fitted line width. Moreover, we established an optimized spectral sampling with the constraint of constant data acquisition time.

2. Methods

2.1. Multistage forward projection

Computing the forward projections is an integral step of the simulation. Several different approaches for projecting a pixel have been proposed [11]. An efficient approximation to the forward projection is the rotation-based projection model [12,13]. Instead of adding the value of a given pixel onto the appropriate location along a rotated projection, the image is rotated and the projection is always taken in the same direction. Forward projection of the spectral-spatial object is mathematically equivalent to a 4D Radon transform. However, direct application of the rotation-based projection approach will require computationally intensive 4D rotations of the synthetic phantom for every gradient magnitude and direction. The algorithm can be accelerated by two orders of magnitude with the adoption of a multistage projection concept: the N-D Radon transform can be treated as a product of $(N-1)$ 2D Radon transforms [14,15]. For example, for a 4D image matrix of N bins in each dimension, the direct 4D Radon transform using M polar, M azimuthal, and M spectral projections will require M^3 4D rotations of the N^4 matrix, whereas the three stage method requires $(MN^2 + M^2N + M^3)$ 2D rotations of N^2 matrices. Fig. 1 illustrates the multistage projection concept for a 3D Radon transform. The relationship between the Radon transform

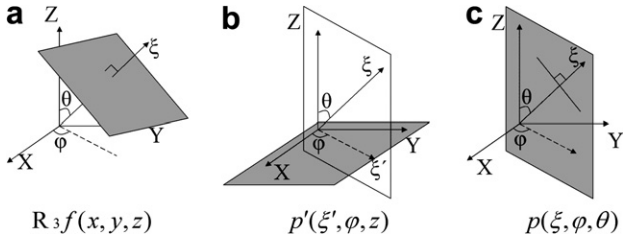

Fig. 1. Diagram illustrating the multistage Radon transform. (a) Integration of an object function $f(x,y,z)$ over the plane perpendicular to an axis determined by a polar angle θ and an azimuthal angle ϕ defines the 3D Radon transform $R_3f(x,y,z)$. This is a projection of the object function onto the line with direction defined by θ and ϕ. (b) A partial Radon transform $p'(\xi',\phi,z)$ is a planar projection of the object function on the plane defined by z-axis and ξ'-axis. The 2D Radon transform is carried out on a stack of horizontal planes perpendicular to z-axis (shaded plane). The ξ'-axis defines a plane (transparent plane) on which the next-stage 2D Radon transform is computed. (c) The 3D Radon transform $p(\xi,\phi,\theta)$ can be obtained from a 2D Radon transform of the partial Radon transform $p'(\xi',\phi,z)$. This is an integral along the line perpendicular to the ξ-axis on the plane defined by the z-axis and the ξ-axis.

$p(\xi,\phi,\theta)$ and a partial Radon transform $p'(\xi',\phi,z)$ is defined as (modified from [16])

$$\begin{aligned}
R_3f(x,y,z) &= \int\int\int_{x,y,z} f(x,y,z)\delta[(x\cos\varphi + y\sin\varphi)\sin\theta \\
&\quad + z\cos\theta - \xi]\,\mathrm{d}x\mathrm{d}y\mathrm{d}z \\
&= \int\int_{\xi',z}\int\int_{x,y} f(x,y,z)\delta(\xi'\sin\theta + z\cos\theta - \xi) \\
&\quad \times \delta(\xi' - x\cos\varphi - y\sin\varphi)\,\mathrm{d}x\mathrm{d}y\mathrm{d}z\mathrm{d}\xi' \\
&= \int\int_{\xi',z}\left[\int\int_{x,y} f(x,y,z)\delta(\xi' - x\cos\varphi - y\sin\varphi)\,\mathrm{d}x\mathrm{d}y\right] \\
&\quad \times \delta(\xi'\sin\theta + z\cos\theta - \xi)\,\mathrm{d}\xi'\mathrm{d}z \\
&= \int\int_{\xi',z} p'(\xi',\varphi,z)\delta(\xi'\sin\theta + z\cos\theta - \xi)\,\mathrm{d}\xi'\mathrm{d}z \\
&= p(\xi,\varphi,\theta), \qquad (1)
\end{aligned}$$

where $R_3f(x,y,z)$ represents a 3D Radon transform of the object function $f(x,y,z)$. From the term in the brackets, the third and fourth line provides a definition of the partial Radon transform $p'(\xi',\phi,z)$. The procedure of a 4D forward projection is split into 3-successive 2D projections, and the simulation of a spectral-spatial EPRI as an 80^4 array is achieved in ~6 min using a PC with a 2 GHz Intel Pentium 4 running MATLAB (Mathworks, Cambridge, MA) version 7.

2.2. Construction of a phantom for EPRI

For EPR imaging of a phantom, we used a sealed borosilicate glass cylinder with 9.5 mm inner diameter and 45 mm length (Fig. 2a). The sensitive region of the resonator was 15 mm in diameter and approximately 25 mm along the axis of the resonator. The bottle was filled with 1 mM deoxygenated OX063 radical (methyl-tris[8-carboxy-2,2,6,6-tetrakis[2-hydroxyethyl]benzo[1,2-d:4,5-

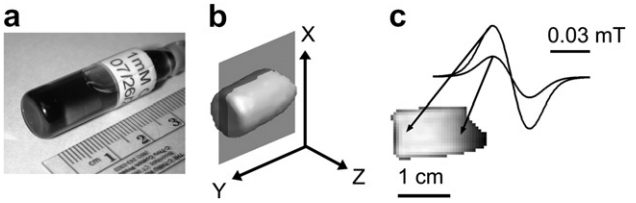

Fig. 2. (a) A sealed borosilicate glass phantom filled with 1 mM deoxygenated OX063 radical. (b) A semi-synthetic phantom was built using an EPR image of the phantom. Both the phantom and the image are oriented with respect to the coordinate system of (b). (c) Signal height is shown as greyscale intensity over a planar section of the shaded vertical region of the image in (b). The left portion of the plane has a relatively uniform, high spectral amplitude distribution. The right part of the image shows a meniscus and a gradual decrease of the signal height due to the fringe field of the resonator. The abrupt edge was defined by a 10% of the maximum signal threshold and an erosion of the outer layer of voxels. To spatial voxels in this synthetic phantom were adjoined the simulated deoxygenated spectra of the OX063 radical with corresponding signal heights as indicated.

d′]bis[1,3]dithiol-4-yl] trisodium salt, MW 1427), a kind gift from Nycomed Innovations, Malmo, SW.

2.3. EPRI procedure

The EPR image was taken using a spectroscopic imager operating at 250 MHz [17]. A single loop-single gap resonator (with a sample holding loop 16 mm in diameter and 15 mm in length) was used with a circulator based bridge with quadrature RF detection. Field modulation was produced by a 7.5 cm radius Helmholtz coil pair operating at 4.98 kHz with over-modulation (17 μT modulation amplitude). The RF power delivered to the resonator was 0.020 mW, which was 10 times lower than the saturation level. Spectral information is obtained from each spatial voxel by applying gradients of different magnitude, referred to as spectral projections, to the sample [8]. A spectral angle α is defined as

$$\tan\alpha = G\Delta L/\Delta B, \tag{2}$$

where G is the gradient magnitude, ΔL is the spatial field of view (FOV), ΔB is the spectral FOV [1–3]. Fourteen spectral projections as defined by Eqs. (2) and (3) were employed for each of 10 polar and 10 azimuthal directions to finish the data acquisition in 68 min.

$$\alpha = \frac{\pi}{2} - \frac{\pi}{14}\left(k - \frac{1}{2}\right), \quad k = 1, 2, \ldots, 14. \tag{3}$$

The spatial and spectral FOV was 30 mm and 0.10 mT, which required a maximum gradient of 30 mT/m. The low SNR at higher gradient projections was partially compensated for by signal averaging using the number of averaged projections $N = [(\cos\alpha)^{-1}]$ where the brackets here indicated greatest integer less than the bracketed expression. This is not the ideal $(\cos\alpha)^{-2}$ compensation discussed in [8]. The compensation used has been chosen as the compromise for reasonable acquisition times under the capabilities of the present system. Each sweep was acquired with 256 field points, 3 ms between analog to digital converter latching of the spectral voltage per point, a 3 ms lock-in amplifier time constant, and with a 12-dB/octave lock-in filter. An SR830 lock-in amplifier (Stanford Research Systems, Sunnyvale, CA) was used. Post processing of the data subjected the projections to a Gaussian filter whose width was 3.2 points. The projections were then subsampled to $256/3.2 = 80$ points so that the four-dimensional image could be reconstructed on a late model PC in a reasonable time (<2 min). The reconstruction used cubic B-spline angular interpolation of the sinograms by a factor of 4 and filtered backprojection [18].

2.4. Building the semi-synthetic phantom

The local EPR signal height is a complicated function of multiple factors including the geometry of the spatial spin distribution and the field intensity of RF irradiation. For the comparison of the signal height variation between simulation and experiment, the construction of a real object using analytical functions may be difficult. An alternative approach is to use a digital image of the object. To establish a clear comparison of the signal height variation with various gradient magnitudes and directions, we synthesized a semi-synthetic phantom following the idea of the voxel-based phantom of Zubal and Harrell [19,20]. The relative location of each voxel in the image determined its position in the X, Y, and Z directions, and the voxel amplitude value of the image determined the EPR signal height—the central value of the singly integrated first harmonic signal—at that location.

We constructed the semi-synthetic phantom using an EPR image of the bottle filled with 1 mM OX063 radical. The same EPRI procedure as the above section was used, but we allowed sufficiently long data acquisition time (7.2 h) to obtain a maximally accurate EPR image. Twenty spectral projections as defined by Eqs. (2) and (4) were employed for each of 20 polar and 20 azimuthal directions, which required maximum gradient of 43 mT/m. The spectral angles were chosen to uniformly cover the spectral angle dimension with values chosen as:

$$\alpha = \frac{\pi}{2} - \frac{\pi}{20}\left(k - \frac{1}{2}\right), \quad k = 1, 2, \ldots, 20. \tag{4}$$

After the reconstruction, a 3D EPR signal height image was built from the 4D matrix. We selected voxels with spectral amplitude greater than 10% of the maximum, and eroded one outer layer of the object. For an accurate comparison of gradient-dependent signal heights from the simulation with those from the imager, we used this low threshold to make the semi-synthetic phantom include the weak signals at the fringe field at the edge of the resonator. Fig. 2 shows that the procedure of erosion and threshold recovered the hard edge of the bottle as well as the weak signals from the fringe field of resonator. Every spatial voxel in this 3D EPR signal height image was associated with a simulated deoxygenated spectrum of OX063

radical with a corresponding signal height to produce a noiseless full four-dimensional spectral-spatial synthetic phantom with a uniform Lorentzian line width of 1.5 μT.

Various magnitudes of gradient ranging from 0.04 to 40.3 mT/m were applied to the 1 mM OX063 phantom in X, Y, and Z directions to obtain signal height variation. The application of corresponding gradients was simulated from the forward projection of the semi-synthetic phantom to generate the signal height variation.

2.5. Incorporation of the experimental noise power spectrum

We investigated the structure of the noise process in EPRI using frequency analysis with a Fourier transform. Noise power spectra of the 1 mM OX063 phantom were obtained at gradient magnitudes as defined by Eqs. (2) and (3). Use of the same spatial and spectral FOV as in the above section resulted in gradients ranging from 0.4 to 30 mT/m. For each gradient magnitude, a true signal was estimated from the average of 1000 spectra. Each spectrum was acquired with 256 field points using the same parameters as is stated above, but the gradient-dependent signal averaging was disabled. Subtraction of individual spectra from the averaged spectrum produced corresponding residuals, from which we computed individual noise power spectra. The envelopes of average noise power spectra for these gradient magnitudes were incorporated into the simulation of EPR imaging.

The low SNR at high gradient was partially compensated for by signal averaging in the EPRI. We took into consideration that the noise amplitude is proportional to square root of the data acquisition time, and that the signal height is linearly proportional to the data acquisition time. A Gaussian random noise for the simulation was generated so that the SNR of the lowest gradient, high SNR spectrum was equal to the experiment. We adjusted the amplitude of the noise by the number of signal averages obtained during the EPRI. Gaussian noise, however, did not fully characterize the experimental noise spectrum. The power spectrum of the Gaussian white noise, produced by a pseudo random number generator, is flat, whereas the experimental noise power spectrum has a characteristic "pink noise" shape. This is determined by the frequency response of the imaging system. To account for the real noise spectrum, we generated a white or Gaussian noise array from the MATLAB function RANDN, subjected this to a Fast Fourier Transform (FFT). This array was multiplied by the envelope or the average of 1000 FFTs of the experimental or deterministic noise obtained as described in the previous paragraph, for each gradient magnitude. The inverse Fourier transform of this array was added to the signals computed from the forward projection of the synthetic phantom. This procedure did not change the SNR but adjusted the shape of the noise power spectrum.

To validate this noise generation procedure, an image obtained from the simulation was compared with that taken from the above EPRI procedure section. Using the same number of sample spectra, we simulated EPRI of the semi-synthetic phantom with uniform signal intensity and with uniform line width. The spectral line width distributions obtained from the simulation were compared with the experiment.

2.6. Measurement of line width resolution and spatial resolution

The performance of EPRI was characterized using line width resolution and spatial resolution. For the measurement of the line width resolution, spatial voxels with spectral amplitude greater than 15% of the maximum were selected. This value was slightly higher than the 10% used in the construction of the semi-synthetic phantom to assure that this data set was a true subset of the semi-synthetic phantom. Each of the spatial voxels had the corresponding EPR spectrum, which was fitted using the line shape simulation algorithm [9,10] to extract the Lorentzian line width. We defined the line width resolution as the standard deviation of the line widths from all of the voxels in the phantom with two outer layers eroded.

The spatial resolution was measured using the 3D EPR signal height image. Any real imaging system produces a more or less blurred image of a source object. This deterministic nonlocal behavior is directly related to the resolving power of the imaging system. For a linear shift-invariant system, spatial resolution is conveniently described in terms of a response or point spread function. To evaluate the spatial resolution of our EPR image, we used the response of our image to the introduction of an edge at which signal appears. This response was obtained along a line perpendicular to the edge. Thus, we modeled the response of the system as the convolution of a Heaviside or step function [21], with a Gaussian point spread function. It is mathematically equivalent to the indefinite integral of the Gaussian point spread function, the error function [22]. Fig. 3 demonstrates the use of the edge

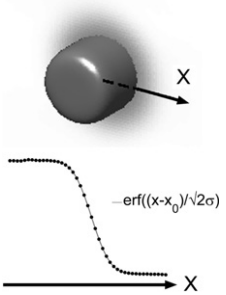

Fig. 3. Measurement of spatial resolution. For this demonstration, we created an analytic cylindrical synthetic phantom and associated the spatial voxels inside the phantom with synthetic EPR spectra of the spin probe. The phantom underwent simulated EPR imaging, and the reconstructed image is shown at the top. A signal height profile along a straight line perpendicular to the surface of the image is plotted at the bottom (dots). The signal height, or edge spread function, is fitted to an error function (smooth line) to extract the FWHM (=2.35 σ) of its derivative.

spread function. The signal height profile along the ray indicated in Fig. 3 was fitted to an error function, from which the full width at half maximum (FWHM) of the point spread function was extracted. The spatial resolution measured in this method is mainly determined by the intrinsic resolution and the finite voxel size of the reconstructed image. With 80 bins for each dimension, the spatial FOV of 30 mm defines the voxel linear dimension of $30\sqrt{2}/80 = 0.53$ mm, which has a non negligible effect on spatial resolution measurement. This voxelation effect was constant with the fixed number of bins (=80) for each dimension. We compared the overall spatial resolution to evaluate the performance of simulated EPRI.

2.7. Parameter optimization

Using the simulation and experiment, we investigated various parameter sets to achieve optimized EPR imaging. First, the accuracy and precision of the fitted line width was examined as a function of field interval. We incremented this from 0.05 to 0.15 mT in 0.01 mT steps. After 14 spectral projections were computed for each of 10 polar and 10 azimuthal directions on the semi-synthetic phantom, we added the noise described in the above section. The reconstruction, fitting, thresholding, and erosion procedure described above produced line width distributions for each sweep width.

We investigated the use of 12, 14, and 16 spectral samples with 10 polar and 10 azimuthal samples to compare the spatial resolution and line width resolution. To examine the intrinsic effect of sampling, simulation was carried out without and with noise included. A constraint of fixed data acquisition time was imposed on the simulations in addition to the experimental noise model described above. Increased sampling requires faster scanning for individual projections to achieve imaging in a fixed time. The noise amplitude was adjusted to be proportional to the inverse square root of the expected data acquisition time for each scan. Experimentally, this data acquisition time constraint was implemented by changing the number of acquired field points. We collected 315, 256, and 205 points (3 ms/point), respectively, for the images with 12, 14, and 16 spectral samples to achieve the same data acquisition time (68 min). Post processing of the data subjected the projections to Gaussian filters whose widths were 3.9 (=315/80) points, 3.2 (=256/80) points, and 2.6 (=205/80) points. The projections were then subsampled to 80 points.

The results presented in the figures and tables regarding this section were collected from 15 repeated simulations and 10 repeated experiments. We displayed the numbers in the format of (mean value) ± (standard error of the mean). When the error bars of $\pm 1.96 \times$ (standard error) do not overlap, the difference is statistically significant with $p < 0.05$ by an unpaired Student t-test [23].

3. Results

3.1. Validation of the observed signal heights

Fig. 4a and b show signal height variation with multiple amplitudes of the gradient applied in X and Y directions. A locus of $\cos\alpha$ is displayed in the dashed line for a relative comparison between the signal heights. In both gradient directions, the signals fell off faster than $\cos\alpha$. This indicates our signal averaging proportional to $(\cos\alpha)^{-1}$ incompletely compensated for the decreased SNR at high gradient projections. The signal height obtained with a gradient applied in the X direction was greater than that obtained with a gradient of the same magnitude applied in the Y direction. Fig. 4c and d show the specific spectra with the gradient of 31.3 mT/m applied in the X and Y directions. The open circles of the plot represent signal heights measured from the 1 mM OX063 phantom in the EPR imager. The solid line represents the signal height variation computed from forward projection of the semi-synthetic phantom. With the cylindrical geometry and the coordinate orientation of Fig. 2, signal height variation in the Z direction was virtually equivalent to that in the X

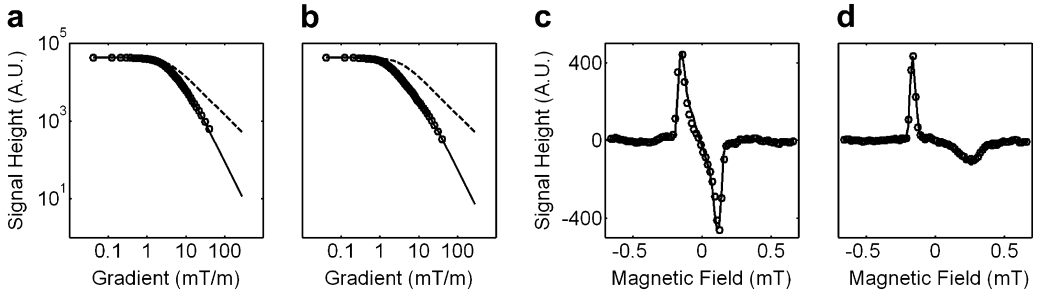

Fig. 4. Comparison of signal heights from experiments (open circles) and computer simulations (solid line) at various gradient strengths. The semi-synthetic phantom and the 1 mM OX063 phantom as described in Fig. 2 were used for the simulation and the experiment. The gradient direction is defined by the coordinate system of Fig. 2. Signal heights were measured as the maximum excursion of the first harmonic line shape. The dashed line represents a locus of $\cos\alpha$ at the corresponding gradient magnitude. Note that $\cos\alpha$ overestimates the signal height. Therefore, $1/\cos\alpha$ will underestimate the number of signal averages necessary to establish equal SNR in the high gradient projections to that of the low gradient projections. Definition of the spectral angle α is given in Eq. (2). (a) Signal heights at various gradient magnitudes applied in the X direction. (b) Signal heights at various gradient magnitudes applied in the Y direction. (c) First harmonic line shape with a gradient of 31.3 mT/m applied in the X direction. (d) First harmonic line shape with a gradient of 31.3 mT/m applied in the Y direction.

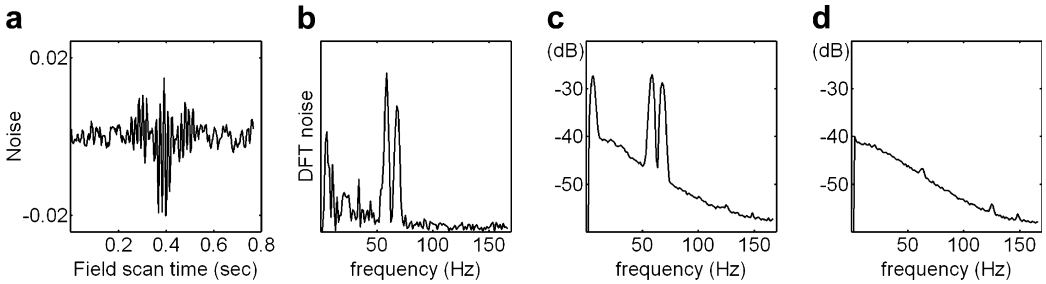

Fig. 5. (a) Noise of the EPR spectrum with the gradient of 0.4 mT/m. A true signal was estimated from the average of 1000 spectra, and the noise was computed by subtracting the true signal from a single spectrum. Noise amplitude is in relative units to the signal height. (b) Discrete Fourier transform of (a) showed two peaks at 55 and 65 Hz referred to as 60 Hz noise. (c) Average of 1000 noise power spectra acquired with the gradient of 0.4 mT/m. (d) Average of 1000 noise power spectra acquired with the gradient of 30 mT/m. Both for (c) and (d), 0 dB corresponds to the noise level that makes signal-to-noise ratio = 1.

direction except for the effects of the fluid meniscus and the asymmetric snout of the phantom.

3.2. Validation of the noise model

Fig. 5 shows the noise profiles of the 1 mM OX063 phantom at the gradients defined by Eqs. (2) and (3). Fig. 5a and b show single residual of the lowest gradient scan and its Fourier transform. Fig. 5c and d show the average of the 1000 noise power spectra for the lowest gradient scan and for the highest gradient scan. Two spikes at 55 and 65 Hz, and another spike near DC were observed in the average noise power spectral density at lowest gradient. These spikes gradually diminished with the increase of the gradient magnitude. The SNR (signal height/rms of residual) of the lowest gradient spectra from the phantom was 420 ± 60 (standard deviation). Using this SNR at the lowest gradient, the relative variation of the noise level was determined accounting for the signal averaging at higher gradient projections.

We compared the simulated image obtained with the above noise model to the image of the phantom taken from the EPR imager. For both images, we used 10 polar, 10 azimuthal, and 14 spectral angle projections. Following the reconstruction and 15% thresholding, the images were fit and eroded by two layers. The threshold generally selected signal from the phantom and eliminated background. Erosion of outer layers of the thresholded object excluded edges of the object which had low signal and which suffered from partial volume averaging that regularly produced line width outliers. Fig. 6a and b show the Lorentzian line width histograms obtained from the experimental EPRI and its simulation. In Fig. 6c, we display a line width histogram from a simulation without noise. Fitting one hundred spectra obtained from the phantom without a gradient resulted in a line width of 1.52 ± 0.01 μT (standard deviation). The semi-synthetic phantom (Fig. 2) was produced using a uniform line width (1.5 μT). The mean line width and the line width resolution from the image of EPRI experiment were 1.79 and 0.17 μT, and were 1.76 and 0.14 μT from the simulation with the noise. The simulation with no noise resulted in a mean line width of 1.76 μT and a line width resolution of 0.10 μT.

3.3. Parameter optimization

The semi-synthetic phantom with uniform line width (1.5 μT) was used to study the effect on resolution of various sweep widths and number of spectral samples. The mean line widths fitted from the simulated EPRI with various sweep widths showed a gradual line width broadening with the increase of sweep width from 0.05 to 0.15 mT as is shown in Fig. 7a. The mean line width resolution improved with the increase of sweep width up to 0.1 mT, and then suffered from a slight degradation when the sweep width was over 0.1 mT to create a gentle minimum (Fig. 7b).

Table 1 shows the variation of the mean line widths of the experimental and simulated images obtained with 12,

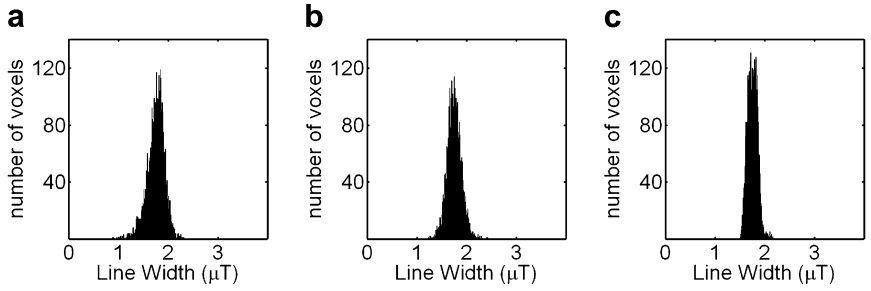

Fig. 6. Histograms of Lorentzian line widths fitted from EPR images. (a) EPR imager. (b) Simulation with the noise model incorporating experimental noise power spectrum. (c) Simulation without noise.

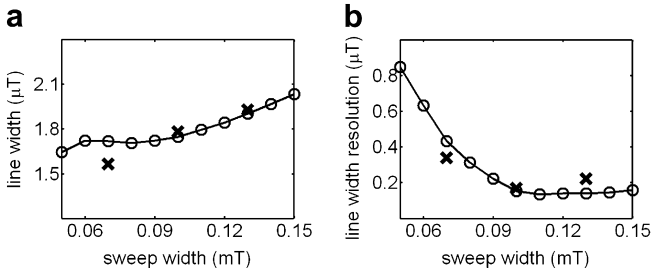

Fig. 7. The effect of sweep width on the line width fitting was studied using both simulation and experiment. Open circles represent results from simulation of the semi-synthetic phantom. Crosses represent results from experiments. (a) Mean line widths. (b) Mean line width resolutions. Standard errors obtained from 15 repeated simulations and 10 repeated experiments were below 1% of each measurement.

Table 1
Mean line widths with 12, 14 and 16 spectral projections

Number of spectral projections	12 (μT)	14 (μT)	16 (μT)
Experiment	1.70 ± 0.01	1.78 ± 0.01	1.77 ± 0.01
Simulation with noise	1.787 ± 0.001	1.756 ± 0.001	1.741 ± 0.001
Simulation without noise	1.787	1.757	1.743

Table 2
Mean line width resolutions with 12, 14 and 16 spectral projections

Number of spectral projections	12 (μT)	14 (μT)	16 (μT)
Experiment	0.24 ± 0.01	0.17 ± 0.01	0.18 ± 0.01
Simulation with noise	0.236 ± 0.001	0.143 ± 0.002	0.144 ± 0.001
Simulation without noise	0.219	0.099	0.063

14, and 16 spectral projections. In the simulation, the increased numbers of spectral projections moved the mean line width slightly closer to the original value of 1.5 μT. In the experiments, values of the mean line widths varied between 1.7 and 1.8 μT with no apparent pattern.

The mean line width resolution shown in Table 2 had a different behavior. Without noise, increase in the number of spectral projections improved the line width resolution. However, the line width resolution from 14 spectral projections was as good as that from 16 spectral projections when the simulation incorporated the experimental noise model and the constraint of fixed data acquisition time. The same pattern was observed in the experiments.

Table 3 summarizes the mean spatial resolution (FWHM) of the simulated images. The simulation showed no significant difference in spatial resolution with the different number of spectral projections with or without noise at the level obtained from our experiments. This differs somewhat from the conclusion from the experiments although the differences between experiments are small.

Table 3
Mean spatial resolution (FWHM) with 12, 14 and 16 spectral projections

Number of spectral projections	12 (mm)	14 (mm)	16 (mm)
Experiment	1.36 ± 0.01	1.43 ± 0.01	1.48 ± 0.01
Simulation with noise	1.49 ± 0.01	1.49 ± 0.01	1.49 ± 0.01
Simulation without noise	1.488	1.484	1.485

4. Discussion

Simulation with the semi-synthetic phantom closely reproduced the experimental signal height variation with various gradient magnitudes as is shown in Fig. 4. The phantom orientation is described in Fig. 2. The cylindrical axis of the phantom was parallel to the Y axis of the coordinate system. Signal heights of the first harmonic projections are primarily influenced by the sharpness of the change in the spectral amplitude at the edge of the phantom. Fig. 2c shows that there is a more gradual change in the spectral amplitude in the Y direction due to the resonator fringe field. At high gradient magnitudes, the soft edge decreases the signal height measured as the maximum excursion of the first harmonic signal. Comparison of Fig. 4a and b shows the corresponding difference in signal heights between the X and Y directions. With a gradient magnitude of 31.3 mT/m in the X direction, the first harmonic signal had a large amplitude in contrast to the amplitude of the line of the same gradient magnitude in the Y direction in that part of the phantom in the fringe field. This is shown in the negative going feature at the right of Fig. 4d. This is the portion of the phantom in the fringe field. The left hand positive going feature is in the high field region of the resonator and has a hard edge similar to that in the radial X direction. Note that this aspect of the experimental projection is fully captured in the forward projection of the semi-synthetic phantom as shown in the solid line in Fig. 4d. The hard edges of the phantom in the constant B_1 portion of the resonator are also well captured as shown in Fig. 4c and d.

Variation of sweep width had a significant effect on the line width fitting (Fig. 7). To reduce the scatter of line width to the level below 0.2 μT, the sweep width should be over 0.1 mT. This corresponds to 6.3 times the peak-to-peak line width of OX063 (0.016 mT), and indicates the minimum sweep width of spectral-spatial image reconstruction for this spin probe. For a proper fitting of the spectrum, we need a substantial portion of the wings of the spectrum as well as the peaks of the first harmonic shape.

Simulation with various numbers of spectral projections revealed an interesting effect when insisting on fixed data acquisition time. In the absence of noise, the increase in spectral projections resulted in a small improvement in image quality as is shown in Tables 1–3. The addition of noise abolishes significant differences in spatial resolution for different numbers of spectral projections. Interestingly, when the experimental noise model was incorporated into the simulation, both 14 spectral projections and 16 spectral projections resulted in the same line width resolutions. The noise modeling of signal averaging proportional to $(\cos\alpha)^{-1}$ will shift data acquisition time to the high

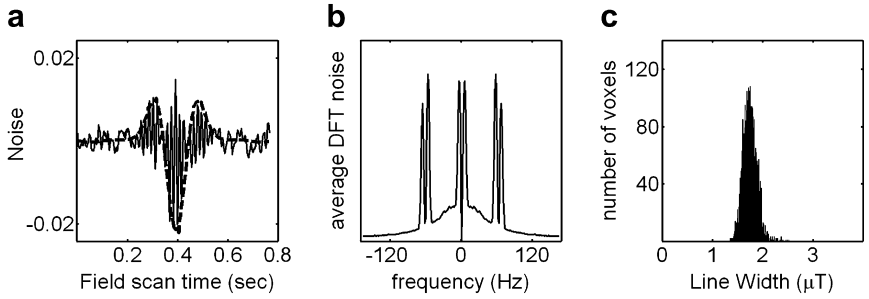

Fig. 8. (a) Noise amplitude at the lowest gradient (0.4 mT/m) was proportional to the derivative of the first harmonic EPR signal (dashed line). (b) Average of 1000 absolute DFT's of the noise at the lowest gradient. The "60 Hz power" line noise is seen as if it were a carrier frequency of amplitude modulation. (c) Histogram of Lorentzian line widths fitted from the EPRI simulation with the 60 Hz noise removed. The lowest gradient SNR was higher than that of Fig. 6b by a factor of three.

gradient projections with the increased number of spectral or gradient amplitude projections. Simulation with a fixed imaging time constraint will raise the noise level for low gradient projections increasing the uncertainty in the spectral fitting when the number of spectral projections is increased. As a result, the difference in the line width resolution as a function of spectral projection number was suppressed, with the particular experimental noise model. The results from experiments showed the same behavior. The increment in spectral projections from 14 to 16 did not improve the line width resolution.

The line width distributions in Fig. 6 indicate that the noise modeling of the simulation achieved comparable performance to the EPR imager. As is shown in Fig. 5, the experimental noise at low gradients had characteristic peaks of 60 Hz noise. This power line noise especially developed its amplitude where the slope of EPR signal was steep, and gradually disappeared as the magnitude of gradient increased (Fig. 5d). At the lowest gradient the envelope of the residual was proportional to the derivative of the first harmonic EPR signal (Fig. 8a). The two peaks near DC in Fig. 8b are from the envelope of the residual, and the 60 Hz noise showed up as if it were a carrier frequency of amplitude modulation. The presence of the 60 Hz could be anticipated from the 3 ms lock-in time constant with a resulting 3 dB pass band of 42 Hz. The 3 ms time constant, in turn, is necessary to minimize distortion of projections while acquiring projections rapidly enough to produce an image in a time short enough for animal imaging.

A closer look at the line width resolution comparison (Table 2) reveals a small but significant superiority of the simulated images to the experimental images. This implies that the experimental noise power spectrum incorporated into the simulation does not explain all distortions from the EPR imager.

As is shown in Fig. 8b, the 60 Hz power line noise comprised a substantial portion of the whole noise. With these characteristic peaks of power line noise removed, the recomputed SNR increased by a factor of three at the lowest gradient. However, this apparent increase in SNR did not improve the line width resolution. Fig. 8c shows the line width histogram obtained from a simulation that removed the power line noise. The mean line width was 1.76 μT, and the line width resolution was 0.14 μT. This is virtually same as the simulation that included the 60 Hz noise (Fig. 6b). It can be inferred that most of the 60 Hz noise was filtered by the spectral fitting procedure. In principle, the noise could be overwhelmed by sampling artifact. That this is unlikely is indicated by the abolition of differences in spatial resolution seen in the noiseless spectra by the addition of noise. The improvement in line width resolution using 16 spectral projections was seen without noise and not with noise. This is due to the poorer SNR of the highest gradient projection with 16 samples, 33.8 mT/m, than the SNR at the highest gradient with 14 spectral samples, 29.6 mT/m. This prediction, verified by experiment, is a major strength of the simulation using this semi-synthetic phantom.

5. Conclusions

Understanding the performance of an EPR imaging system is difficult to predict from general rules concerning EPRI system performance. The characteristics, particularly the noise characteristics of each individual system must be incorporated into model projections. This must then be simulated using a combination of the signal from the discrete Radon transform of the object and the noise characteristics measured in each system. Spectral-spatial EPRI was simulated using a 4D Radon transform incorporating the experimental noise power spectrum. We validated the signal height variation with gradients of different magnitudes and directions. The noise model of the simulation achieved the same performance of the EPR imager with respect to line width distribution. Simulation is a powerful tool that enables a well controlled search for an optimized parameter set. Using the simulation, we established a proper sweep width and spectral sampling specific to our EPR imaging system.

Acknowledgments

This work was supported by NIH Grants CA98575 and EB002034. Useful discussions with Drs. Xiaochuan Pan and Charles A. Pelizzari are gratefully acknowledged.

References

[1] P.C. Lauterbur, D.N. Levin, R.B. Marr, Theory and simulation of NMR spectroscopic imaging and field plotting by projection reconstruction involving an intrinsic frequency dimension, J. Magn. Reson. 59 (1984) 536–541.

[2] M.M. Maltempo, Differentiation of spectral and spatial components in EPR imaging using 2-D image reconstruction algorithms, J. Magn. Reson. 69 (1986) 156–161.

[3] S.S. Eaton, M.M. Maltempo, E.D.A. Stemp, G.R. Eaton, Three-dimensional EPR imaging with one spectral and two spatial dimensions, Chem. Phys. Lett. 142 (1987) 567–569.

[4] A. Sotgiu, K. Mader, G. Placidi, S. Colacicchi, C.L. Ursini, M. Alecci, pH-sensitive imaging by low-frequency EPR: a model study for biological applications, Phys. Med. Biol. 43 (1998) 1921–1930.

[5] P. Kuppusamy, H.Q. Li, G. Ilangovan, A.J. Cardounel, J.L. Zweier, K. Yamada, M.C. Krishna, J.B. Mitchell, Noninvasive imaging of tumor redox status and its modification by tissue glutathione levels, Cancer Res. 62 (2002) 307–312.

[6] M. Elas, B.B. Williams, A. Parasca, C. Mailer, C.A. Pelizzari, M.A. Lewis, J.N. River, G.S. Karczmar, E.D. Barth, H.J. Halpern, Quantitative tumor oxymetric images from 4D electron paramagnetic resonance imaging (EPRI): methodology and comparison with blood oxygen level-dependent (BOLD) MRI, Magn. Reson. Med. 49 (2003) 682–691.

[7] A. Matsumoto, S. Matsumoto, A.L. Sowers, J.W. Koscielniak, N.J. Trigg, P. Kuppusamy, J.B. Mitchell, S. Subramanian, M.C. Krishna, K. Matsumoto, Absolute oxygen tension (pO2) in murine fatty and muscle tissue as determined by EPR, Magn. Reson. Med. 54 (2005) 1530–1535.

[8] B.B. Williams, X.C. Pan, H.J. Halpern, EPR imaging: the relationship between CW spectra acquired from an extended sample subjected to fixed stepped gradients and the Radon transform of the resonance density, J. Magn. Reson. 174 (2005) 88–96.

[9] B.H. Robinson, C. Mailer, A.W. Reese, Linewidth analysis of spin labels in liquids. I. Theory and data analysis, J. Magn. Reson. 138 (1999) 199–209.

[10] C. Mailer, B.H. Robinson, B.B. Williams, H.J. Halpern, Spectral fitting: the extraction of crucial information from a spectrum and a spectral image, Magn. Reson. Med. 49 (2003) 1175–1180.

[11] R.H. Huesman, G.T. Gullberg, W.L. Greenberg, T.F. Budinger, User Manual, Donner Algorithms for Reconstruction Tomography, Lawrence Berkeley Laboratory, University of California, 1977.

[12] E. DiBella, A. Barclay, R. Eisner, R. Schaefer, A comparison of rotation-based methods for iterative reconstruction algorithms, IEEE Trans. Nucl. Sci. 43 (1996) 3370–3376.

[13] J.W. Wallis, T.R. Miller, An optimal rotator for iterative reconstruction, IEEE Trans. Med. Imaging 16 (1997) 118–123.

[14] C.M. Lai, P.C. Lauterbur, A gradient control device for complete 3-dimensional nuclear magnetic-resonance zeugmatographic imaging, J. Phys. E. Sci. Instrum. 13 (1980) 747–750.

[15] R.K. Woods, W.B. Hyslop, R.B. Marr, P.C. Lauterbur, Image reconstruction, in: G.R. Eaton, S.S. Eaton, K. Ohno (Eds.), EPR Imaging and In Vivo EPR, CRC Press, Inc., Boca Raton, 1991, pp. 91–118.

[16] Z.-P. Liang, P.C. Lauterbur, Principles of Magnetic Resonance Imaging, IEEE Press, New York, 2000.

[17] H.J. Halpern, M.K. Bowman, D.P. Spencer, J.V. Polen, E.M. Dowey, R.M. Massoth, A.C. Nelson, B.A. Teicher, An imaging radiofrequency electron spin resonance spectrometer with high resolution and sensitivity for in vivo measurements, Rev. Sci. Instrum. 60 (1989) 1040–1050.

[18] K.-H. Ahn, H.J. Halpern, Comparison of local and global angular interpolation applied to spectral-spatial EPR image reconstruction, Med. Phys. 34 (2007) 1047–1052.

[19] I.G. Zubal, C.R. Harrell, Voxel based Monte Carlo calculations of nuclear medicine images and applied variance reduction techniques, Image Vision Comput. 10 (1992) 342–348.

[20] I.G. Zubal, C.R. Harrell, E.O. Smith, Z. Rattner, G. Gindi, P.B. Hoffer, Computerized three-dimensional segmented human anatomy, Med. Phys. 21 (1994) 299–302.

[21] R.N. Bracewell, The Fourier Transform and Its Applications, third ed., McGraw Hill, Boston, 2000.

[22] H.H. Barrett, W. Swindell, Radiological Imaging, revised ed., Academic Press, New York, 1981.

[23] P.R. Bevington, D.K. Robinson, Data Reduction and Error Analysis, third ed., McGraw-Hill, Boston, 2003.